

Electric field control of interaction between magnons and quantum spin defects

Abhishek B. Solanki,^{1,2,*} Simeon I. Bogdanov,^{1,2,3,4} Avinash Rustagi,¹ Neil R. Dilley,² Tingting Shen,^{5,2} Mohammad M. Rahman,¹ Wenqi Tong,¹ Punyashloka Debashis,^{1,2,6} Zhihong Chen,^{1,2} Joerg Appenzeller,^{1,2} Yong P. Chen,^{5,1,2,7,8,9,10} Vladimir M. Shalaev,^{1,2,7,10} and Pramey Upadhyaya^{1,2,7,10,†}

¹*School of Electrical and Computer Engineering,
Purdue University, West Lafayette, IN 47906, USA*

²*Birck Nanotechnology Center, Purdue university, West Lafayette, IN 47906, USA*

³*Department of Electrical and Computer Engineering,
University of Illinois at Urbana-Champaign, IL 60801, USA*

⁴*Nick Holonyak, Jr. Micro and Nanotechnology Laboratory,
University of Illinois at Urbana-Champaign, IL 61801, USA*

⁵*Department of Physics and Astronomy, Purdue University, West Lafayette, IN 47906, USA*

⁶*Components Research, Intel Corporation, Hillsboro, Oregon 97124, USA*

⁷*Purdue Quantum Science and Engineering Institute (PQSEI),
Purdue University, West Lafayette, IN 47906, USA*

⁸*Institute of Physics and Astronomy and Villum Center for Hybrid Quantum
Materials and Devices, Aarhus University, 8000 Aarhus-C, Denmark*

⁹*WPI-AIMR International Research Center for Materials Sciences, Tohoku University, Sendai 980-8577, Japan*

¹⁰*The Quantum Science Center (QSC), a National Quantum Information
Science Research Center of the U.S. Department of Energy (DOE)*

(Dated: May 26, 2021)

Hybrid systems coupling quantum spin defects (QSD) and magnons can enable unique spintronic device functionalities and probes for magnetism. Here, we add electric field control of magnon-QSD coupling to such systems by integrating ferromagnet-ferroelectric multiferroic with nitrogen-vacancy (NV) center spins. Combining quantum relaxometry with ferromagnetic resonance measurements and analytical modeling, we reveal that the observed electric-field tuning results from ferroelectric polarization control of the magnon-generated fields at the NV. Exploiting the demonstrated control, we also propose magnon-enhanced hybrid electric field sensors with improved sensitivity.

Introduction— Hybrid platforms that combine distinct physical systems with complementary characteristics provide a unique playground to explore phenomena and device functionalities richer than their components [1–4]. Optically active quantum spin defects (QSDs), i.e. *microscopic* spin impurities in insulating hosts, coupled with magnons, i.e. the elementary collective excitations of *macroscopically* ordered magnetic systems, have recently emerged as one such promising hybrid spin system [5–24].

The motivation for creating magnon-QSD systems is twofold. First, magnons resonantly enhance microwave fields up to nanoscale [5], feature long-distance nonreciprocal transport [25] and mode confinement at reconfigurable nanoscale magnetic textures [26–28]—properties that have given birth to the burgeoning field of magnonics [29]. Therefore, magnons provide promising control fields for solving the challenge of on-chip coherent driving [5, 6, 17, 30] and communication between QSD qubits [7, 8, 31]. Second, application of well-established quantum defect magnetometry techniques to magnon-generated fields provides route to develop previously unavailable noninvasive and nanoscale probes for a broad range of magnetic phenomena [5–24].

Electric field control of spin system is a key resource in spintronics. Adding such electric-field control to QSD-magnon coupling would thus expand the range of phe-

nomena and device functionalities that can be enabled by magnon-QSD hybrid systems. For example, the dependence of magnon-spin coupling on an applied electric field, when combined with the magnetometry of magnon-generated fields, provides a new scheme for sensing electric fields and phenomena via QSDs. Apart from extending the reach of QSD-based nanoscale sensors [32] to probe magnetoelectric materials, the attractive feature offered by this approach includes leveraging magnetic resonance enhancement [9] and the stronger magnetic field susceptibility of QSD ground state [33] to enhance the electric field sensitivity. On another front, electric fields, as opposed to magnetic fields and currents, can be confined to the scale of inter-qubit separation with minimal Joule heating [17, 34–36]. Electric field tuning of QSD-magnon interaction could thus enable a scalable network of QSD-based circuits, where the desired spins are driven and/or entangled with their neighbors via locally tunable magnon modes.

In this Letter, we experimentally demonstrate electric-field control of interaction between magnons and QSDs by engineering a new hybrid system that combines a ferroelectric-ferromagnetic multiferroic [37–40] with QSDs. We also propose and show theoretically that the demonstrated electric field control can be used to sense electric fields with nearly 2-orders of magnitude improvement in the sensitivity when compared with sensing

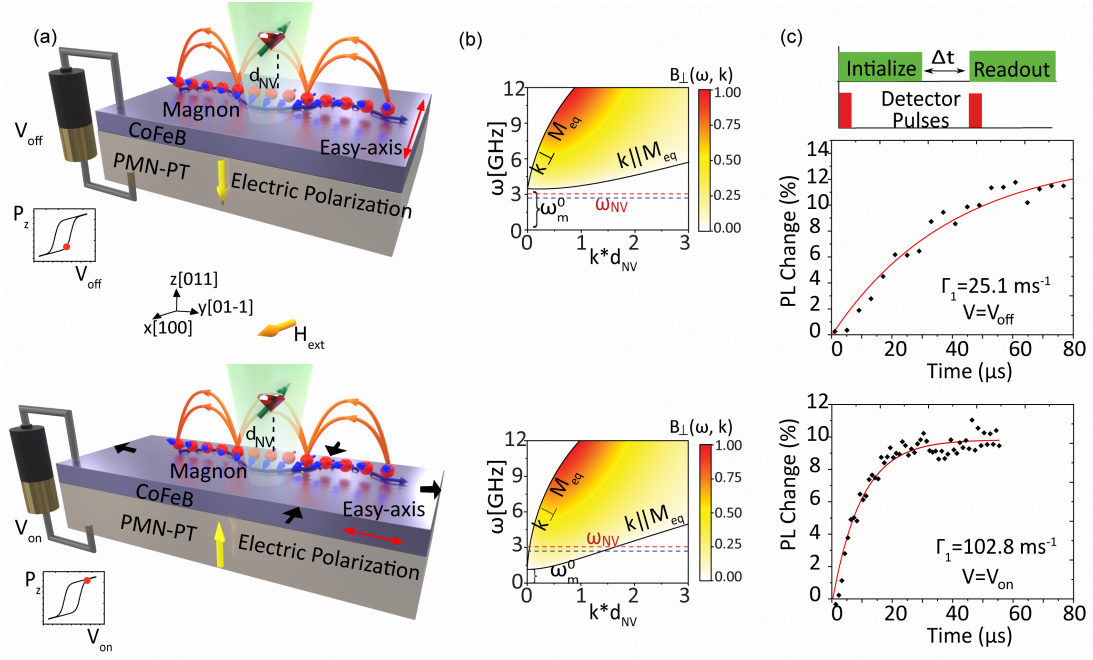


FIG. 1. (a) Schematic illustration of the QSD-magnon hybrid system. An external voltage V controls the electrical polarization of PMN-PT (as shown in schematic P-V loops) resulting in lattice strain and change in lateral dimensions of the device structure. The direction of the magnetic anisotropy field (easy axis—red double arrows) is along x for $V = V_{off}$ and along y for $V = V_{on}$ in CoFeB. (b) Maps of normalized $B_{\perp}(k)$ as a function of $\omega - k$ for both V_{off} and V_{on} . The black lines enveloping the colormap are the calculated magnon dispersion lines for bulk modes ($k \parallel M$) and surface modes ($k \perp M$). The dashed coloured lines represent the NV ESR lines ω_{NV} . (c) Change in relaxation rates of the NV ensembles enabled by electrical tuning of QSD-magnon coupling. The schematic diagram represents the pulse sequence of the measurement scheme.

schemes utilizing direct coupling of ground-states of QSD with electric fields. While electric-field control of magnetism in such composite multiferroics has garnered significant attention in the classical domain [37, 38], our results highlight their utility for enabling functional quantum hybrid systems.

Central Scheme—The device structure and the central scheme are depicted in Fig. 1(a). We disperse nanodiamonds with NV center [41] ensembles, which act as QSDs, onto ferromagnetic (FM) (20nm) CoFeB/(300 μ m, 011-cut) ferroelectric (FE) PMN-PT composite multiferroic films [39, 40]. The magnons in CoFeB produce oscillating dipole magnetic fields at the NV, whose magnitude and frequencies (ω_m) depends on their wavevector (k) [10]. The components of these fields that are transverse to the NV-quantization axis mediate the interaction between magnons and the NV-spins via Zeeman coupling. The central idea we demonstrate here is that by controlling the ferroelectric polarization component P_z along the [011] axis in PMN-PT, magnon bands in CoFeB film can be moved with respect to the NV ESR transitions. This brings magnon-generated fields of different magnitude in resonance with the NV ESR transitions, thereby enabling electric-field control of the magnon-QSD interaction.

We show in Fig. 1(a) the particular case of how the magnon bands respond to the flipping of P_z from $-z$ to

$+z$ direction in the presence of a fixed external magnetic field (H_{ext}) along the [100] x -axis. The reversal of P_z is initiated at $V = V_{off}$, where the magnon bands and NV ESR transitions are off resonance, giving rise to a weak coupling. In contrast, for $V = V_{on}$ the reversal is nearly completed, and the magnon bands and NV ESR transitions are brought into the resonance, giving rise to a stronger coupling.

The above movement of magnon bands results from the coupled electric, elastic and magnetic orders in the multiferroic and can be understood as following. The (011)-cut PMN-PT features piezo-electric coefficients d_{31} and d_{32} of opposite signs. Consequently, to accommodate the increasing P_z , PMN-PT expands along the [01-1] y -axis and shrinks along the [100] x -axis. The transfer of this anisotropic strain to CoFeB, when combined with the magnetoelastic interaction, lowers (raises) energy for the magnetization oriented along the y (x) axis. This change in the electric polarization-controlled uniaxial magnetic anisotropy results in the easy-axis reorienting from x to y for P_z changing from $-z$ to $+z$ [39, 40]. Crucially, both the magnon band gap $\omega_m^0 \equiv \omega_m(k=0)$ and hence the frequency range spanned by the magnon bands depend on the magnetic anisotropy [42]. The alignment of the direction of H_{ext} with the easy axis maximizes ω_m^0 , while their orthogonal orientation minimizes ω_m^0 . Con-

sequently, as the voltage is increased from V_{off} to V_{on} the magnon bands are pulled to lower frequencies and brought into resonance with the NV ESR transitions [see Fig. 1(b)].

To demonstrate and quantify the electric-field control of magnon-QSD interaction in these hybrids we perform NV-relaxometry [41] measurements in presence of thermal magnons (see Methods in Supplementary). At room temperature, our NV ensembles [43] feature an intrinsic relaxation rate of $\Gamma_0 \approx 3 [ms]^{-1}$ due to electron-phonon interaction and paramagnetic impurities in the vicinity of NVs [41]. The coupling to the thermal magnons acts as a source of additional magnetic noise for the NV spins. This results in an increased NV spin relaxation rate (Γ_1), which thus provides a measure of the magnon-QSD coupling. In the remainder of this Letter, we demonstrate that in NV/CoFeB/PMN-PT hybrid films magnon bands can be moved in and out of resonance with NV ESR transitions via application of the electric field. This is measured as a 400% tuning of Γ_1 by voltage [Fig. 1(c)] in qualitative agreement with theory. We also show theoretically that this change in Γ_1 can be improved by multiple orders of magnitude by patterning and using low damping ferromagnets, which we propose to leverage for improving electric field sensing by NV.

Anisotropic QSD-magnon coupling.—We begin by understanding the role of a *static* magnetic anisotropy field on NV-spin magnon coupling. To this end, we measure the relaxation rate Γ_1 for H_{ext} applied along the [100] x -axis and the [01-1] y -axis of the (011-cut) PMN-PT [Fig. 2(a,b)]. For the field applied along the x -axis, Γ_1 decreases monotonically reaching the minimum value of $18.7 \pm 2 [ms]^{-1}$ for $H_{ext} = 180G$. On the other hand, for the field applied along the y -axis, Γ_1 increases first reaching a maximum value of $262.4 \pm 29 [ms]^{-1}$ at $H_{ext} = 50G$ and then decreases. The relaxation of NV-spins coupled to magnons is governed by the spectral density of magnon-generated transverse field fluctuations evaluated at the NV ESR transitions [10]. The thermally populated modes of the magnetic film $\omega_m(k)$ generate a magnetic noise with the spectral density given by [10] (read Supplementary Materials: S4)

$$G_m(\omega) = \int B_{\perp}^2(k) D[\omega, \omega_m(k)] n[\omega_m(k)] Adk / (2\pi)^2, \quad (1)$$

Here, B_{\perp} is the magnitude of the transverse magnetic field at the NV due to a magnon occupying the mode with wavevector k (whose relative magnitude is shown in Fig. 1b), $D = \alpha\omega_m/\pi [(\omega - \omega_m)^2 + \alpha^2\omega_m^2]$ is the magnon spectral density with α being the Gilbert damping parameter, and $nAdk/2\pi^2$ counts the total number of thermal magnons occupying the states in the neighbourhood of k , where A is the area of the film and $n = k_B T / \hbar\omega_m$ is the Rayleigh-Jeans distribution function with k_B and

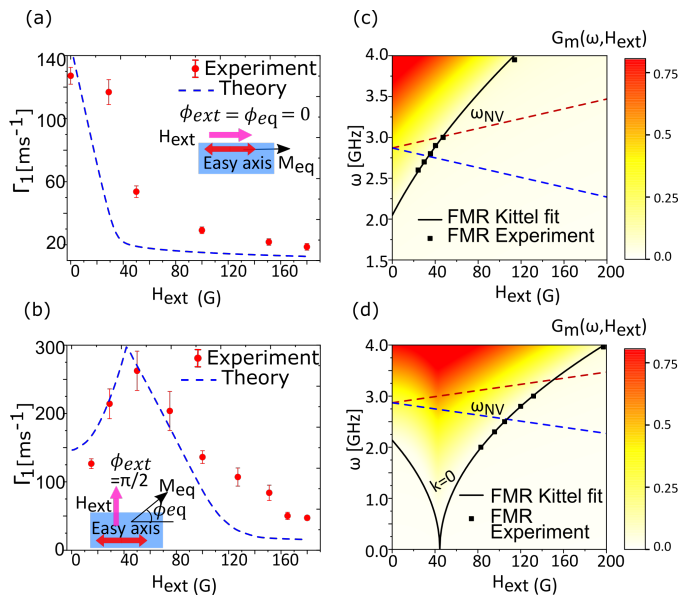


FIG. 2. (a), (b) Measured relaxation rate Γ_1 as a function of external magnetic field H_{ext} applied parallel (x -axis) and orthogonal (y -axis) to the magnetic anisotropy field (easy-axis) respectively. The dashed lines represent theoretical fits of relaxation rates Γ_1 . The inset shows the schematic variation of H_{ext} w.r.t the easy-axis and the direction of equilibrium magnetization. (c), (d) Ferromagnetic resonance (FMR) frequency (ω_m) as a function of external magnetic field H_{ext} fitted with the Kittel formula for 20nm CoFeB film (solid lines) for H_{ext} parallel (x -axis) and orthogonal (y -axis) to the anisotropy field respectively. The dashed coloured lines represent maximum spread of the NV ESR lines ω_{NV} . The color map represents the calculated values of the magnetic noise spectral density $G_m(\omega, H_{ext})$ for an effective NV height $d_{NV} = 77nm$.

T being the Boltzman constant and temperature, respectively. External magnetic field tunes the spectral density of magnetic noise resonant with the NV ESR transitions by controlling the magnon spectrum.

The magnon spectrum in thin films is described by the dipole-exchange spin waves [44], which can be written in the form $\omega_m(k) = \omega_m^0 + f(k)$. Here, ω_m^0 (Kittel mode) is the band gap at $k = 0$ and $f(k)$ (see Supplementary Materials: S4) describes the nondegenerate branches of dispersion [c.f. magnon bands in Fig. 1(b)]. To track the location of magnon bands, in Fig. 2(c, d), we present the results of ferromagnetic resonance (FMR) experiments on our multiferroic films, which directly measure ω_m^0 as a function of H_{ext} along the x and y axis (see details in Supplementary Materials: S1). Consistent with our relaxometry measurements, ω_m^0 also depends on the orientation of H_{ext} , lying at a higher frequency for $H_{ext} \parallel x$ when compared with that for $H_{ext} \parallel y$. This anisotropic behavior can be described by considering a uniaxial magnetic anisotropy energy of the form $\mathcal{F}_{an} = H_k M_s (m_y^2 - m_x^2) / 2$ [37, 39, 40] in the magnetic film. Here, M_s is the satu-

ration magnetization, m_x and m_y are the x and y components of the unit vector oriented along the magnetization, and H_k parameterizes the strength of the uniaxial anisotropy field. When $H_k > 0$ ($H_k < 0$), the easy axis is oriented along the x (y) axis. In such films, ω_m^0 is governed by the Kittel formula [42]:

$$\omega_m^0 = \gamma \sqrt{H_1 H_2}, \quad (2)$$

with $H_1 = H_{ext} \cos(\phi_{ext} - \phi_{eq}) + 2H_k \cos 2\phi_{eq}$ and $H_2 = H_{ext} \cos(\phi_{ext} - \phi_{eq}) + H_k \cos 2\phi_{eq} + 4\pi M_s$. Here, ϕ_{ext} and ϕ_{eq} are the azimuthal angles of the external magnetic field and the equilibrium magnetization, respectively [see inset Fig. 2(a,b)]. The Kittel formula fits are shown in Fig. 2(c,d), which gives $H_k = 20G$ with the easy-axis oriented along the x -axis. The central result highlighted by these fits is that ω_m^0 and thus the magnon bands shift monotonically to higher frequencies for H_{ext} parallel to the x -axis. In contrast, for H_{ext} along the y -axis, ω_m^0 and the band frequencies are pulled down first, before rising to higher values.

Equipped with the magnon spectrum, we plot the normalized field dependent noise spectral density $G_m(\omega, H_{ext})$, along with the maximum spread of NV ensemble ESR frequencies $\omega_{max}^+ = 2.87 + \gamma H_{ext}[GHz]$ and $\omega_{min}^- = 2.87 - \gamma H_{ext}[GHz]$ in Figs. 2(c) and 2(d) (see Supplementary Materials: S4). For $H_{ext} \parallel x$, magnons generating higher B_\perp are pushed away from the frequency range probed by the NV ensemble due to the monotonic shift of magnon bands to higher frequency with H_{ext} [see Fig. 1(b)]. As a result, for $H_{ext} \parallel x$, $G_m(\omega, H_{ext})$ within ω_{max}^+ and ω_{min}^- decreases monotonically, consistent with the relaxation rate's decrease with the field. Whereas, for $H_{ext} \parallel y$, since ω_m^0 is first pushed to lower frequencies for $H_{ext} < 50G$ before moving to higher frequencies for $H_{ext} > 50G$, magnons with stronger B_\perp are brought into (out of) resonance with NV ensemble ESR transitions for $H_{ext} < 50G$ ($H_{ext} > 50G$). Consequently, $G_m(\omega, H_{ext})$ within ω_{max}^+ and ω_{min}^- and the relaxation rates increase (decrease) with H_{ext} for $H_{ext} < 50G$ ($H_{ext} > 50G$).

Theoretical best fits of relaxation rate (see Supplementary Materials: S4) are also shown in Fig. 2(a, b) exhibiting qualitative agreement with the experimental results. Quantitative differences may arise from neglecting finite mode ellipticity for magnons [10, 20], two-magnon scattering-induced NV-relaxation [15], and/or effect of local inhomogeneities (arising, for example, from local strain) on the magnon spectrum.

Electric field control.—The multiferroic hybrid offers the attractive property of moving magnon spectrum with electric field by *dynamically* tuning the magnetic anisotropy. In Fig. 3(a), we show $\omega_m^0(V)$ for $H_{ext} = 57G$ along with $H_k(V)$ (see inset) extracted by applying Kittel formula Eq. 2 on the measured $\omega_m^0(V)$ (see Supplementary Materials: S1). The $H_k(V)$ inherits the char-

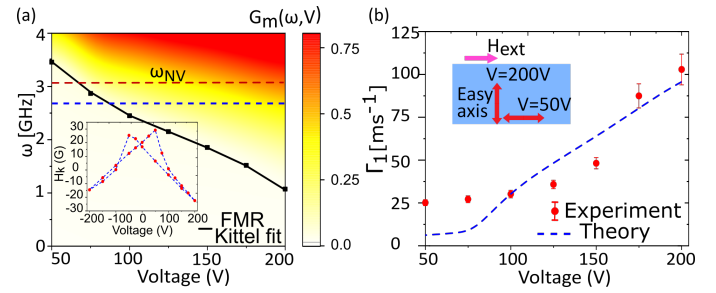


FIG. 3. (a) FMR frequency (ω_m^0) (data in black lines) as a function of applied voltage extracted from the experimental results for a fixed external magnetic field $H_{ext} = 57G$ along x -axis. The color map represents the calculated values of the magnetic noise spectral density $G_m(\omega, V)$ for an effective NV height $d_{NV}=77nm$. The dashed coloured lines represent maximum spread of the NV ESR lines ω_{NV} . The inset shows the detailed measurements of magnetic anisotropy field as a function of applied voltage. We begin by polling the ferromagnet to (-200V) and then change the voltage in steps towards +200V. Following this, the measurement is performed by changing the voltage in reverse direction from 200V to -200V. (b) Measured relaxation rates Γ_1 as a function of applied voltage for a fixed $H_{ext} = 57G$ along x -axis. The inset shows a schematic illustration of magnetic anisotropy field for the two different voltages for a fixed H_{ext} . The dashed line represents theoretical fit of relaxation rates Γ_1 .

acteristic butterfly-shaped curve of anisotropic strain as a function of applied voltage, which is the hallmark of coupled ferroelectric, elastic and magnetic order tuning the anisotropy in FM/FE multiferroics [37, 39, 40]. Particularly, as the voltage is increased from 50V to 200V, H_k decreases monotonically from $H_k = 30G$ at $V=50V$ to $H_k = -22G$ at $V = 200V$. Notably, this maximal change in H_k corresponds to the flipping of the easy axis from x to y consistent with flipping of P_z in PMN-PT (see Supplementary Materials: S2). Correspondingly, we observe the largest $\omega_m^0 = 3.45GHz$ when the easy-axis is aligned with the direction of H_{ext} for $V=50V$. Conversely, ω_m^0 decreases to the minimum value $1.07GHz$ when the easy-axis is aligned orthogonal to the direction of H_{ext} at $V=200V$. In the following, we focus on this polarization flipping-induced changes in NV-spin and magnon coupling.

We obtain the normalized field dependent magnetic noise spectral density $G_m(\omega, V)$ shown in Figs. 3(a) by substituting the electric field-dependent magnon spectrum from FMR experiments into Eq. 1 (see Supplementary Materials: S4). On the same figure we also depict the NV ESR frequencies, which lie within the dashed horizontal lines $\omega_{max}^+(H_{ext} = 57G)$ and $\omega_{min}^-(H_{ext} = 57G)$ and remain unaffected by applied electric field. For $V=50V$, i.e. P_z points downward, the $\omega_m^0 = 3.45GHz$ is the largest for our hybrids and lies above the NV transition frequency [Fig. 3(a)] [as shown in Fig. 1(b), where we referred to $V=50V$ as V_{off}]. Consequently, magnons

are off-resonant with NVs and are expected to couple weakly with them, which is reflected in the low value of calculated $G_m(\omega, V)$ within ω_{max}^+ and ω_{min}^- band at $V=50V$. As the voltage is increased, the polarization of PMN-PT is reoriented, H_k and ω_m^0 decrease and magnons with stronger dipole fields are brought into the resonance with the NV ESR transitions [see Fig. 1]. As a result, the magnons interact strongly with the NV spins. This increased coupling is reflected in $G_m(\omega, V)$ increasing monotonically and reaching the maximum value within the frequency range spanned by ω_{max}^+ and ω_{min}^- for $V = 200V$; we thus refer to $V = 200V$ as V_{on} .

The experimentally measured spin relaxation rate indeed increases monotonically as the voltage varies from V_{off} to V_{on} [see Fig. 3(b)], showing good agreement with the above qualitative picture. Namely, the lowest relaxation rate of $25.1 \pm 2 [ms]^{-1}$ is observed for $V = V_{off}$ which increases monotonically to $102.8 \pm 9 [ms]^{-1}$ at $V = V_{on}$. The corresponding optical spin contrast curves are shown in Fig. 1(c). Finally, we also plot the results of theoretical Γ_1 fits for the NV ensembles, with the nanodiamond orientation found in the previous section (see Supplementary Materials: S4). The theoretical fits are in reasonable quantitative agreement with the experiments. In addition to the reasons pointed out for Fig. 2(a, b), the quantitative difference between experiment and theory in this case may arise from additional inhomogeneous magnon-scattering potentials introduced by ferroelectric domains due to domain-nucleation mechanism of ferroelectric switching [45] which can be addressed by using NV-scanning geometry [19]. Furthermore, we also performed control experiments with hybrid structures of NV-ensembles coupled with PMN-PT substrate without CoFeB film (Supplementary Materials: S3) and observed no measurable voltage modulation of the NV relaxation time.

Discussion.—The observed shift in NV’s relaxation rates, Γ_1 , can be exploited for sensing E-fields (hereafter, ‘magnon-sensing’). To quantify the performance of magnon-sensing, we compare its expected single-spin DC E-field sensitivity to the sensing schemes based on direct coupling of NV’s ESR levels [46] to the DC electric field (hereafter, ‘direct-sensing’). The sensitivity of magnon-sensing and direct-sensing schemes scales as $S \propto 1/\eta\sqrt{T_\chi}$ [47]; (see Supplementary Materials: S5). Here, η is the transduction parameter, which for the magnon-sensing (direct-sensing) is given by $\eta_m = \partial\Gamma_1/\partial E$ (η_d =Stark shift [46]), and T_χ is the time scale before which unwanted signals dephases or relaxes the NV-spin. For direct-sensing, $\eta_d \sim 28Hz/(V/cm)$ [46] and T_χ ms is the NV’s decoherence time, which yields photon shot noise-limited single-spin DC field sensitivities $S_d \sim 890(V/cm)/\sqrt{Hz}$ [46]. For our experiments, $\eta_m \sim 15Hz/(V/cm)$ and $T_\chi = 1/\Gamma_1$ 10 μs from the high voltage bias region of Fig. 3(b). This suggests that the sensitivity of the magnon-sensing scheme S_m , is an order of magnitude poorer than

S_d for the parameter regime we study here. However, since η_m is not limited by the weak Stark shifts, S_m can be improved by several orders of magnitude by properly designing the ferromagnet as we highlight next.

The transduction parameter for magnon-sensing can be written as $\eta_m = \nu\beta$, where $\beta \equiv \partial\omega_m/\partial E$ parameterizes the shift in magnon modes due to E-field, and the dimensionless factor $\nu \equiv \partial\Gamma_1/\partial\omega_m$ represents the change in the NV-relaxation corresponding to the shift of magnon modes. β is governed by the piezoelectric and magneto-elastic properties of the CoFeB/PMN-PT stack, which can be read from Fig. 3(a) to be $\sim 0.5MHz/(V/cm)$, about four orders larger than η_d . Therefore, small ($\sim 15Hz/(V/cm)$) values of η_m in our present hybrids arises from $\nu \ll 1$. Physically, $\nu \ll 1$ means that a broad band of magnons must be moved before NV and magnons become off-resonant [c.f. Fig. 1(b)], resulting in slow variation of Γ_1 with frequency.

In nanoscale magnets (instead of films) the magnon modes are discretized due to confinement [48]. Consequently, a much smaller shift in the magnon frequency ($\sim \alpha\omega_m$) would make the magnon mode and the NV ESR off-resonant, hence enhancing ν . Additionally, choosing a smaller α would further enhance ν . Informed by these heuristics, we calculate S_m for low damping CoFeB [49, 50] nanomagnet/PMN-PT hybrids, yielding minimum sensitivity $S_m \sim 1(V/cm)/\sqrt{Hz}$ (see Supplementary Materials: S5). Other knobs to improve S_m include choosing magnets with larger magneto-elastic coefficients (β), such as Terfanol-D [37, 51] and/or lower Gilbert damping (α) such as YIG [52] and VTCN [53]. Furthermore, our proposed scheme can also leverage various other mechanisms for electric field control of magnetism [34, 35] such as voltage control of interfacial magnetic anisotropy and magneto-ionic effect to enhance β .

In summary, leveraging coupled ferroelectric, lattice, magnetic and spin degrees of freedom, we demonstrated dynamic tuning of magnon and QSD interaction by electric fields. As an example application of the demonstrated control, we also proposed magnetic resonance-enhanced electric field sensors. Our relaxometry data suggests that the QSD relaxation can be used as a non-invasive probe of ferroelectric state via magnetoelectric coupling. Future research extending the present study to the scanning NV geometry [24] could thus extend the advantages of NV-center probing of condensed matter [32] to multiferroics and a broad range of magnetoelectric phenomena studied in spintronics. Beyond sensing, an array of QSD/nano-FM/FE [54, 55] hybrids could provide a novel approach to build scalable QSD-based quantum circuits. In such circuits, selective driving of QSD-qubits by a weak global microwave drive, and tunable transfer of information between such qubits, can potentially be activated electrically by tuning the magnon frequency of nano-FMs in proximity to the desired qubits.

Acknowledgements — This work was supported in

part by NSF Award 1838513, NSF Award 1944635, NSF 2015025-ECCS and the U.S. Department of Energy, Office of Science through the Quantum Science Center (QSC), a National Quantum Information Science Research Center.

* solanka@purdue.edu

† prameyup@purdue.edu

- [1] G. Kurizki, P. Bertet, Y. Kubo, K. Mølmer, D. Petrosyan, P. Rabl, and J. Schmiedmayer, *PNAS* **112**, 3866 (2015).
- [2] D. Lachance-Quirion, Y. Tabuchi, A. Gloppe, K. Usami, and Y. Nakamura, *Applied Physics Express* **12**, 070101 (2019).
- [3] Y. Li, W. Zhang, V. Tyberkevych, W. Kwok, A. Hoffmann, and V. Novosad, *Journal of Applied Physics* **128**, 130902 (2020).
- [4] D. D. Awschalom, C. H. R. Du, R. He, J. Heremans, A. Hoffmann, J. Hou, H. Kurebayashi, Y. Li, L. Liu, V. Novosad, J. Sklenar, S. Sullivan, D. Sun, H. Tang, V. Tyberkevych, C. Trevillian, A. W. Tsen, L. Weiss, W. Zhang, X. Zhang, L. Zhao, and C. W. Zollitsch, *IEEE Transactions on Quantum Engineering*, 1 (2021).
- [5] P. Andrich, F. Charles, X. Liu, H. L. Bretscher, J. R. Berman, F. J. Heremans, P. F. Nealey, and D. D. Awschalom, *npj Quantum Information* **3**, 28 (2017).
- [6] D. Kikuchi, D. Prananto, K. Hayashi, A. Laraoui, N. Mizuochi, M. Hatano, E. Saitoh, Y. Kim, C. A. Meriles, and T. An, *Applied Physics Express* **10**, 103004 (2017).
- [7] L. Trifunovic, F. L. Pedrocchi, and D. Loss, *Physical review X* **3**, 041023 (2013).
- [8] B. Flebus and Y. Tserkovnyak, *Phys. Rev. B* **99**, 140403 (2019).
- [9] L. Trifunovic, F. L. Pedrocchi, S. Hoffman, P. Maletinsky, A. Yacoby, and D. Loss, *Nature nanotechnology* **10**, 541 (2015).
- [10] T. Van der Sar, F. Casola, R. Walsworth, and A. Yacoby, *Nature communications* **6**, 7886 (2015).
- [11] M. Page, B. A. McCullian, C. Purser, J. G. Schulze, T. M. Nakatani, C. S. Wolfe, J. R. Childress, M. E. McConney, B. M. Howe, P. C. Hammel, and V. P. Bhallamudi, *Journal of Applied Physics* **126**, 124902 (2019).
- [12] C. Wolfe, S. Manuilov, C. Purser, R. Teeling-Smith, C. Dubs, P. Hammel, and V. Bhallamudi, *Applied Physics Letters* **108**, 232409 (2016).
- [13] H. Zhang, M. J. H. Ku, F. Casola, C. H. R. Du, T. van der Sar, M. C. Onbasli, C. A. Ross, Y. Tserkovnyak, A. Yacoby, and R. L. Walsworth, *Physical Review B* **102**, 024404 (2020).
- [14] C. Du, T. Van der Sar, T. X. Zhou, P. Upadhyaya, F. Casola, H. Zhang, M. C. Onbasli, C. A. Ross, R. L. Walsworth, Y. Tserkovnyak, *et al.*, *Science* **357**, 195 (2017).
- [15] B. McCullian, A. M. Thabt, B. Gray, A. Melendez, M. S. Wolf, V. Safonov, D. Pelekhov, V. Bhallamudi, M. Page, and P. Hammel, *Nature communications* **11** (2020), 10.1038/s41467-020-19121-0.
- [16] T. X. Zhou, J. J. Carmiggelt, L. M. Gächter, I. Esterlis, D. Sels, R. J. Stöhr, C. Du, D. Fernandez, J. F. Rodriguez-Nieva, F. Büttner, *et al.*, arXiv preprint arXiv:2004.07763 (2020).
- [17] D. Labanowski, V. Bhallamudi, Q. Guo, C. Purser, B. McCullian, P. Hammel, and S. Salahuddin, *Science advances* **4**, eaat6574 (2018).
- [18] B. Flebus and Y. Tserkovnyak, *Phys. Rev. Lett.* **121**, 187204 (2018).
- [19] A. Finco, A. Haykal, R. Tanos, F. Fabre, S. Chouaieb, W. Akhtar, I. Robert-Philip, W. Legrand, F. Ajejas, K. Bouzehouane, *et al.*, arXiv preprint arXiv:2006.13130 (2020).
- [20] A. Rustagi, I. Bertelli, T. Van der Sar, and P. Upadhyaya, *Physical review B* **102** (2020), 10.1103/PhysRevB.102.220403.
- [21] S. Chatterjee, J. F. Rodriguez-Nieva, and E. Demler, *Phys. Rev. B* **99**, 104425 (2019).
- [22] C. Purser, V. Bhallamudi, F. Guo, M. Page, Q. Guo, G. Fuchs, and P. Hammel, *Applied Physics Letters* **116**, 202401 (2020).
- [23] C. Gonzalez-Ballester, T. Van der Sar, and O. Romero-Isart, arXiv preprint arXiv:2012.00540 (2020).
- [24] L. Thiel, Z. Wang, A. Tschudin, D. Rohner, I. Gutiérrez-Lezama, N. Ubrig, M. Gibertini, E. Giannini, F. Morpurgo, and P. Maletinsky, *Science* **364**, 973 (2019).
- [25] R. Damon and J. Eshbach, *Journal of Physics and Chemistry of Solids* **19**, 3 (1960).
- [26] K. Wagner, A. Kákay, K. Schultheiss, A. Henschke, T. Sebastian, and H. Schultheiss, *Nature nanotechnology* **11**, 432 (2016).
- [27] N. Nagaosa and Y. Tokura, *Nature nanotechnology* **8**, 899 (2013).
- [28] V. Sluka, T. Schneider, R. Gallardo, *et al.*, *Nature nanotechnology* **14**, 328 (2019).
- [29] A. V. Chumak, V. I. Vasyuchka, A. A. Serga, and B. Hillebrands, *Nature Physics* **11**, 453 (2015).
- [30] X. Wang, Y. Xiao, C. Liu, *et al.*, *npj Quantum Information* **6** (2020), 10.1038/s41534-020-00308-8.
- [31] M. Fukami, D. Candido, D. Awschalom, and M. Flatté, arXiv preprint arXiv:2101.09220 (2021).
- [32] F. Casola, T. van der Sar, and A. Yacoby, *Nature Reviews Materials* **3**, 17088 (2018).
- [33] Y. Dovzhenko, F. Casola, S. Schlotter, T. Zhou, F. Büttner, R. Walsworth, G. Beach, and A. Yacoby, *Nature communications* **5** (2014), 10.1038/ncomms5065.
- [34] F. Matsukura, Y. Tokura, and H. Ohno, *Nature nanotechnology* **10**, 209 (2015).
- [35] U. Bauer, L. Yao, A. Tan, P. Agrawal, S. Emori, H. Tuller, and G. Van Dijken, S. amd Beach, *Nature Materials* **14**, 174 (2015).
- [36] A. Laucht, J. Muhonen, F. Mohiyaddin, R. Kalra, J. Dehollain, S. Freer, F. Hudson, M. Veldhorst, R. Rahman, G. Klimeck, K. Itoh, D. Jamieson, J. McCallum, A. Dzurak, and A. Morello, *Science Advances* **1**, e1500022 (2015).
- [37] N. Sun and G. Srinivasan, *SPIN* **2** (2012), 10.1142/S2010324712400048.
- [38] R. Ramesh and N. A. Spaldin, *Nature Materials* **6**, 21–29 (2007).
- [39] S. Zhang, Y. Zhao, X. Xiao, Y. Wu, S. Rizwan, L. Yang, P. Li, J. Wang, M. Zhu, H. Zhang, X. Jin, and X. Han, *Scientific Reports* **4** (2015), 10.1038/srep03727.
- [40] T. Shen, V. Ostwal, K. Camsari, and J. Appenzeller, *Scientific Reports* **10** (2020), 10.1038/s41598-020-67776-y.

- [41] M. Doherty, N. Manson, P. Delaney, F. Jelezko, J. Wrachtrup, and L. Hollenberg, *Physics Reports* **528** (2013), [10.1016/j.physrep.2013.02.001](https://doi.org/10.1016/j.physrep.2013.02.001).
- [42] C. Kittel, *Phys. Rev.* **73**, 155 (1948).
- [43] S. Bogdanov, M. Shalaginov, A. Akimov, A. Lagutchev, P. Kapitanova, J. Liu, D. Woods, M. Ferrera, P. Belov, J. Irudayaraj, A. Boltasseva, and V. Shalaev, *Physical Review B* **96**, 035146 (2017).
- [44] B. Kalinikos and A. Slavin, *Journal of Physics C: Solid State Physics* **19**, 7013 (1986).
- [45] P. Li, Y. Zhao, S. Zhang, A. Chen, D. Li, J. Ma, Y. Liu, D. Pierce, J. Unguris, H. Piao, H. Zhang, M. Zhu, X. Zhang, X. Han, M. Pan, and C. Nan, *ACS Appl. Mater. Interfaces* **9**, 2642–2649 (2017).
- [46] F. Dolde, H. Fedder, M. Doherty, T. Nöbauer, F. Rempp, G. Balasubramanian, T. Wolf, F. Reinhard, L. Hollenberg, F. Jelezko, and J. Wrachtrup, *Nature Physics* **7**, 459–463 (2011).
- [47] C. Degen, F. Reinhard, and P. Cappellaro, *Rev. Mod. Phys.* **89** (2017), [10.1103/RevModPhys.89.035002](https://doi.org/10.1103/RevModPhys.89.035002).
- [48] F. Guo, L. M. Belova, and R. D. McMichael, *Physical review letters* **110**, 017601 (2013).
- [49] A. Lee, J. Brangham, Y. Cheng, S. White, W. Ruane, D. Esser, B.D. McComb, P. Hammel, and F. Yang, *Nature communications* **8** (2017), [10.1038/s41467-017-00332-x](https://doi.org/10.1038/s41467-017-00332-x).
- [50] M. Schoen, D. Thonig, M. Schneider, T. Silva, H. Nembach, O. Eriksson, K. O., and J. Shaw, *Nature Physics* **12** (2016), [10.1038/nphys3770](https://doi.org/10.1038/nphys3770).
- [51] M. Liu, S. Li, Z. Zhou, S. Beguhn, J. Lou, F. Xu, T. J. Lu, and N. X. Sun, *Journal of Applied Physics* **112** (2012), [10.1063/1.4754424](https://doi.org/10.1063/1.4754424).
- [52] M. C. Onbasli, A. Kehlberger, D. Kim, G. Jakob, M. Kläui, A. Chumak, B. Hillebrands, and C. Ross, *APL Materials* **2** (2014), [10.1063/1.4896936](https://doi.org/10.1063/1.4896936).
- [53] A. Franson, N. Zhu, M. Kurfman, S. Chilcote, D. Candido, K. Buchanan, M. Flatté, H. X. Tang, and E. Johnston-Halperin, *APL Materials* **7** (2019), [10.1063/1.5131258](https://doi.org/10.1063/1.5131258).
- [54] A. Chen, Y. Zhao, Y. Wen, L. Pan, P. Li, and X. Zhang, *Science Advances* **5**, eaay5141 (2019).
- [55] A. Biswas, H. Ahmad, J. Atulasimha, and S. Bandyopadhyay, *Nano Letters* **17**, 3478–3484 (2017).